Unraveling information about supranuclear-dense matter from the complete binary neutron star coalescence process using future gravitational-wave detector networks

Anna Puecher[1,2], Tim Dietrich[3,4], Ka Wa Tsang[1,2,5], Chinmay Kalaghatgi[1,2,6],
Soumen Roy[1,2], Yoshinta Setyawati[1,2], Chris Van Den Broeck[1,2]

[1]*Nikhef – National Institute for Subatomic Physics,*
Science Park 105, 1098 XG Amsterdam, The Netherlands
[2]*Institute for Gravitational and Subatomic Physics (GRASP),*
Utrecht University, Princetonplein 1, 3584 CC Utrecht, The Netherlands
[3]*Institut für Physik und Astronomie, Universität Potsdam,*
Haus 28, Karl-Liebknecht-Str. 24/25, 14476, Potsdam, Germany
[4]*Max Planck Institute for Gravitational Physics (Albert Einstein Institute), Am Mühlenberg 1, Potsdam, Germany*
[5]*Van Swinderen Institute for Particle Physics and Gravity,*
University of Groningen, Nijenborgh 4, 9747 AG Groningen, The Netherlands
[6]*Institute for High-Energy Physics, University of Amsterdam,*
Science Park 904, 1098 XH Amsterdam, The Netherlands
(Dated: October 18, 2022)

Gravitational waves provide us with an extraordinary tool to study the matter inside neutron stars. In particular, the postmerger signal probes an extreme temperature and density regime and will help reveal information about the equation of state of supranuclear-dense matter. Although current detectors are most sensitive to the signal emitted by binary neutron stars before the merger, the upgrades of existing detectors and the construction of the next generation of detectors will make postmerger detections feasible. For this purpose, we present a new analytical, frequency-domain model for the inspiral-merger-postmerger signal emitted by binary neutron stars systems. The inspiral and merger part of the signals are modeled with `IMRPhenomD_NRTidalv2`, and we describe the main emission peak of postmerger with a three-parameter Lorentzian, using two different approaches: one in which the Lorentzian parameters are kept free, and one in which we model them via quasi-universal relations. We test the performance of our new complete waveform model in parameter estimation analyses, both with simulated signals and numerical relativity waveforms. We investigate the performance of different detector networks to determine the improvement that future detectors will bring to our analysis. We consider Advanced LIGO+ and Advanced Virgo+, KAGRA, and LIGO-India. We also study the possible impact of a detector with high sensitivity in the kilohertz band like NEMO, and finally we compare these results to the ones we obtain with third-generation detectors, the Einstein Telescope and the Cosmic Explorer.

I. INTRODUCTION

Neutron stars (NSs) can reach extremely high densities, creating conditions that cannot be reproduced by laboratory experiments. Hence, they provide a perfect environment to study supranuclear-dense matter and its Equation of State (EoS). Until a few years ago, the study of NSs was limited to electromagnetic (EM) observations, but since the first detection of a gravitational wave (GW) signal from a binary neutron star (BNS), GW170817 [1], GWs provide new ways to study NSs and their mergers. Since the EoS determines the NS's macroscopic properties, such as its mass, radius, and tidal deformability, it can be constrained by measuring the imprint it leaves in the GW signal emitted during the coalescence [2, 3].

Up to now, Advanced LIGO [4] and Advanced Virgo [5] detected two BNS systems, GW170817 [1, 6] and GW190425 [7]. These detections already allowed to put constraints on the supranuclear-dense matter EoS, which was possible since the GW signal emitted during the inspiral phase provides information about the EoS through tidal deformability measurements [2, 8–16]. While the uncertainty on current measurements is still large, the higher sensitivies of future generation detectors such as

the Einstein Telescope (ET) [17–23] or the Cosmic Explorer (CE) [24, 25] will significantly improve them.

In addition to a more detailed analysis of the inspiral, 3rd generation (3G) GW detectors are also expected to detect GWs from the postmerger phase of the BNS coalescence [26–30]. This is of special interest, since the postmerger probes a different density and temperature regime than the inspiral, with densities higher than the ones of the binary component stars, and temperatures large enough so that also the effect of different transport coefficients will start to impact the data [31–33].

Unfortunately, postmerger studies pose numerous challenges. Firstly, the postmerger part of the observed GW signal is expected to be noticeably weaker than the inspiral one, since detectors are limited by quantum noise at the high frequencies, where the postmerger emission is strongest [34–38]. The dedicated searches for GWs emitted by a possible remnant of GW170817 [39, 40] found no evidence of such a signal, and showed that with the sensitivity of Advanced LIGO and Advanced Virgo the source distance should have been at least one order of magnitude less for the postmerger signal to be detectable. Secondly, postmerger physics includes thermal effects, magnetohydrodynamical instabilities, neutrino emission, dissipative

processes, and possible phase transitions [41–47], which make the postmerger particularly difficult to model, but, on the other hand, allow us to investigate a variety of interesting physical processes. Because of the complexity of the evolution, the study of the postmerger relies heavily on numerical-relativity (NR) simulations, which, however, are also limited due to their high computational cost and the fact that it is currently not possible to take into account all the physical processes that influence the postmerger.

Nonetheless, previous studies based on NR simulations showed some common key features of the postmerger GW spectrum, finding in some cases universal relations with the NS properties [35–38, 48–56], and some efforts have been made also to construct full inspiral, merger and postmerger models for BNS coalescences. Also morphology-independent analyses of the postmerger GW signal have been proposed in [50, 55, 57], while in [58] a hierarchical model to generate postmerger spectra was developed. With a different approach, [59–61] construct analytical models for the postmerger signal, based on features found in NR simulated waveforms. Breschi *et al.* in [62] proposed a frequency-domain model for the postmerger, built with a combination of complex Gaussian wavelets, and showed in [63] how this model performs using a 3G detector network. Wijngaarden *et al.* [64] build a hybrid model, using analytical templates for the premerger phase and a morphology-independent analysis, based on sine-Gaussian wavelets, for the postmerger one. This approach allows to study the BNS signal with all the data available, and also to perform consistency tests between the pre- and postmerger results.

Following similar ideas, in this paper we construct a phenomenological frequency domain model for the entire BNS coalescence consisting of the inspiral, merger, and postmerger phase. Our final aim is it to employ the developed model for parameter estimation analyses. To model the coalescence during the inspiral up to the merger, we rely on `IMRPhenomD_NRTidalv2` [65]. The postmerger phase is modelled with a three-parameter Lorentzian describing the main emission peak of its spectrum, following Tsang *et al.* [66]. For the Lorentzian, we use two different approaches: in one case, we compute the parameters from quasi-universal relations, describing them as a function of the BNS's properties, in the other one, we treat them as free parameters. The advantage of having a full analytical model is that it can be directly employed by existing parameter estimation pipelines; see e.g. [67, 68].

This paper is structured as follows. In Sec.II we describe how our model is built, the methods used for parameter estimation, and the detectors we consider. Results are shown in Sec. III, and conclusions are presented in Sec. IV. Appendix A is devoted to mismatch calculations between our models and the NR waveforms, while in Appendix B we show the results obtained specifically with our postmerger model with free Lorentzian parameters.

II. METHODS AND SETUP

We construct a frequency-domain waveform model to describe the full inspiral, merger, and postmerger of a BNS coalescence. In this section, we describe how we model the postmerger part of the signal, and how we connect it to the inspiral-merger model to obtain the full waveform. We then describe the framework used for data analysis, explaining how we speed up parameter estimation using relative binning, the analysis setup, the BNS sources that we study, and the employed detector networks to determine to what extent future detector networks will enable postmerger studies.

A. Inspiral-merger-postmerger model construction

Multiple studies have shown that the postmerger GW spectrum includes various strong peaks [35–38, 48, 51–54, 69]. For simplicity, we limit ourselves to the main emission peak at a frequency f_2, which corresponds to the dominant GW frequency; see e.g. [48]. Following this approach, the postmerger can be described in time domain by a simple damped sinusoidal waveform [66], whose Fourier transform is a Lorentzian. Therefore, in frequency domain, we model the postmerger with a three-parameter Lorentzian

$$h_{22}(f) = \frac{c_0 c_2}{\sqrt{(f - c_1)^2 + c_2^2}} e^{-i \arctan\left(\frac{f - c_1}{c_2}\right)}, \quad (1)$$

where c_0 corresponds to the maximum value, c_1 to the dominant emission frequency f_2, and c_2 to the inverse of the damping time, which sets the Lorentzian's width.

We determine the coefficients c_i with two different approaches: (I) we treat them as free parameters, and try to measure c_0, c_1, and c_2 together with the other BNS's properties; and (II) we compute the c_i coefficients from quasi-universal relations that describe them as functions of the system's parameters. Depending on its properties and EoS, a given BNS could undergo a prompt collapse to a black hole (BH), hence without a postmerger emission. In this scenario, while in case (I) we expect that the values recovered for the free parameters reflect the absence of a postmerger signal, in (II) the quasi-universal relations employed might lead to a bias in the estimation of the binary's intrinsic parameters. For this reason, we ideally want to use the Lorentzian model with quasi-universal relations only when we know that a postmerger emission is present. Since the threshold mass for a prompt collapse is EoS dependent and still unknown, following [59] we assume that a BNS system undergoes prompt collapse if the tidal polarizability parameter κ_2^T is lower than a threshold value $\kappa_{thr} = 40$. The quantity κ_2^T is defined as

$$\kappa_2^T = 3 \left[\Lambda_2^A (X_A)^4 X_B + \Lambda_2^B (X_B)^4 X_A \right], \quad (2)$$

where $\Lambda_2^j = \frac{2}{3} k_2 \left(R_j / M_j \right)^5$ with $j \in \{A, B\}$ are the dimensionless tidal deformabilities, and $X_j = M_j / M$. Here

k_2 is the dimensionless $\ell = 2$ Love number, R_j and M_j are respectively the radius and gravitational mass of the individual stars, and $M = M_A + M_B$ is the BNS's total mass[1].

1. Quasi-universal relations for the Lorentzian parameters

For the approach introduced as method (II), we use quasi-universal relations, i.e. phenomenological relations that are independent of the EoS, to constrain the coefficients c_i in Eq. (1). This provides a direct connection between the Lorentzian coefficients and the BNS's properties.

Since the postmerger Lorentzian model extends the waveform used for inspiral and merger beyond its merger frequency f_{merg}, a straightforward way to find the value of c_0 is by rescaling the amplitude of the `IMRPhenomD_NRTidalv2` waveform at merger $\mathcal{A}_{\mathrm{NRTidalv2}}(f_{\mathrm{merg}})$. Specifically, we use

$$c_0 = \sigma \times \mathcal{A}_0 \times \mathcal{A}_{\mathrm{NRTidalv2}}(f_{\mathrm{merg}}), \qquad (3)$$

where $\mathcal{A}_0$ is the mass and distance scaling factor employed in `IMRPhenomD` [71]. The prefactor σ is added to obtain a better calibration to the NR waveforms, and we set $\sigma = 10.0$, which gives the lowest mismatch values (the definition of mismatch and details about its computation are provided in Appendix A).

Since c_1 represents the dominant postmerger oscillation frequency f_2, we resort to the fit in Eq. (8) of [66]

$$M c_1(\zeta) = \beta \frac{1 + A\zeta}{1 + B\zeta}, \qquad (4)$$

with $\beta = 3.4285 \times 10^{-2}$, $A = 2.0796 \times 10^{-3}$, and $B = 3.9588 \times 10^{-3}$. The parameter ζ is

$$\zeta = \kappa_{\mathrm{eff}}^T - 131.7010 \frac{M}{M_{\mathrm{TOV}}}. \qquad (5)$$

In the last equation, $\kappa_{\mathrm{eff}}^T = 3/18 \tilde{\Lambda}$, with $\tilde{\Lambda}$ being the binary's mass-weighted tidal deformability

$$\tilde{\Lambda} = \frac{16}{3} \frac{(M_A + 12 M_B) M_A^4 \Lambda_A + (M_B + 12 M_A) M_B^4 \Lambda_B}{(M_A + M_B)^5}. \qquad (6)$$

Although ζ, and therefore c_1, in Eq. (5) is a function of the maximum mass allowed for a non-rotating stable NS M_{TOV}, which depends on the specific EoS, we fix $M_{\mathrm{TOV}} = 2 M_\odot$ for this work.

With this choice for c_0 and c_1, a model for c_2 is built from a set of 48 non-spinning NR waveforms, from the CoRe database [72, 73]. For this, we first find the values

of c_2 that minimize the mismatch of the Lorentzian waveform and the NR waveform between $0.75\, c_1$ and 8192 Hz using a flat noise power spectral density (PSD); see Appendix A for details. The flat PSD ensures that no high-frequency information is suppressed in the match computation. For each waveform, c_2 minimization is performed using the `L-BFGS-B`, `SLSQP`, `TNC` and `Powell` methods available in `SciPy` [74] and the value of c_2 with the least mismatch value is used. It was seen that c_2 showed a similar trend against $\kappa_{\mathrm{eff}}^T q^2$, with $q = M_A/M_B$ the mass ratio, as c_1 does against ζ. Hence, a analogous ansatz was used to perform a fit. However, using the parameters obtained from doing a simple curve fit showed unphysical amplitude behaviour for a few of the NR waveforms. For further tuning, the mismatch was minimized for all the NR waveforms by varying the fit parameters and the parameters that gave the least mismatch were then recorded and added to the model. The functional form of c_2 and the values obtained for the fit parameters in this manner are

$$c_2 = 2 + \gamma \frac{1 + C \kappa_{\mathrm{eff}}^T q^2}{1 + D \kappa_{\mathrm{eff}}^T q^2}, \qquad (7)$$

with $\gamma = 19.4579017$, $C = -9.63390738 \times 10^{-4}$, and $D = 6.45926154 \times 10^{-5}$.

2. The full waveform

To obtain a model describing the full coalescence, the previously derived postmerger model is connected to the waveform describing the inspiral and merger part of the signal, for which we use the phenomenological waveform `IMRPhenomD_NRTidalv2` [65].

Amplitude: To ensure a smooth transition between the two models, we apply a Planck-taper window α:

$$\alpha = \begin{cases} 0 & \text{for } f < f_{\mathrm{tr}}, \\ \exp\left[\frac{f_{\mathrm{end}} - f_{\mathrm{tr}}}{f - f_{\mathrm{tr}}} + \frac{f_{\mathrm{end}} - f_{\mathrm{tr}}}{f - f_{\mathrm{end}}} + 1\right]^{-1} & \text{for } f_{\mathrm{tr}} < f < f_{\mathrm{end}}, \\ 1 & \text{for } f > f_{\mathrm{end}}. \end{cases} \qquad (8)$$

The window is applied just before the frequency of the main postmerger peak f_2, which corresponds to our model's parameter c_1. The value of the window's starting frequency f_{tr} is chosen to ensure a good match with NR waveforms. In particular, in Ref. [66] one of the time-domain features identified in the postmerger signal morphology is the *first postmerger minimum*, which corresponds to a clear amplitude minimum present shortly after the merger, before the amplitude starts increasing again. By comparison with NR waveforms in the CoRe database [72, 73], we found that this feature is best reproduced by our model when the Planck window is applied between $f_{\mathrm{tr}} = 0.75\, c_1$ and $f_{\mathrm{end}} = 0.9\, c_1$. Following [71],

---

[1] See also [70] for more updated relations which were not yet available when we started our work.

we add an exponential correction factor $\exp\left[-\frac{p(f-c_1)}{c_2}\right]$ to the Lorentzian amplitude, in order to smoothen possible kinks arising when going to the time domain. We set $p = 0.01$, which is enough to reduce the kink, but not so large that it significantly influences the merger amplitude.

Phase: To ensure that the waveform phase is C^1 continuous, we introduce two coefficients a and b, writing the phase as

$$\phi_{\text{IM}}(f) = \phi_{\text{Lor}}(f) + a + bf, \qquad (9)$$

with ϕ_{IM} the phase of `IMRPhenomD_NRTidalv2` waveform and $\phi_{\text{Lor}} = \arg(h_{22}(f))$ the Lorentzian one.

The values of a and b are computed at the same transition frequency $f_{\text{tr}} = 0.75\, c_1$ at which we start the Planck-taper window for the amplitude, such that

$$\left.\frac{d\phi_{\text{IM}}}{df}\right|_{f_{\text{tr}}} = \left.\frac{d\phi_{\text{Lor}}}{df}\right|_{f_{\text{tr}}} + b, \qquad (10)$$

$$\phi_{\text{IM}}(f_{\text{tr}}) = \phi_{Lor}(f_{\text{tr}}) + bf_{\text{tr}} + a. \qquad (11)$$

$$\tilde{h}(f) = \begin{cases} \mathcal{A}_{\text{IM}}(f)e^{i\phi_{\text{IM}}} & \text{for } f < f_{\text{tr}}, \\ \left(\mathcal{A}_{\text{IM}}(f) + \alpha\mathcal{A}_{\text{Lor}}(f)e^{-\frac{p(f-c_1)}{c_2}}\right)e^{i(\phi_{\text{Lor}}+bf+a)-i2\pi\Delta t f} & \text{for } f > f_{\text{tr}}, \end{cases} \qquad (13)$$

where $\mathcal{A}_{\text{IM}}(f)$ and $\phi_{\text{IM}}(f)$ are respectively the amplitude and phase of the `IMRPhenomD_NRTidalv2` waveform, and $\mathcal{A}_{\text{Lor}} = |h_{22}(f)|$ the amplitude of the Lorentzian one.

B. Parameter estimation

In the following, we focus on how to recover the source's parameters given the detector data d and under the hypothesis of a specific model $\mathcal{H}$ used to describe the waveform. In a Bayesian framework, this corresponds to evaluating the posterior $p(\vec{\theta}|\mathcal{H}, d)$, which, according to Bayes' theorem, is

$$p(\vec{\theta}|\mathcal{H}, d) = \frac{p(d|\mathcal{H}, \vec{\theta})p(\vec{\theta}|\mathcal{H})}{p(d|\mathcal{H})}. \qquad (14)$$

In Eq. (14), the prior probability density $p(\vec{\theta}|\mathcal{H})$ encodes our prior knowledge about the source or the model; the evidence $p(d|\mathcal{H})$ describes the probability of observing the data d given the model $\mathcal{H}$, independently of the specific choice of parameters $\vec{\theta}$; and the likelihood $p(d|\mathcal{H}, \vec{\theta})$ represents the probability of observing d with the specific set of parameters $\vec{\theta}$.

The priors chosen for this work are described later in this section, while the evidence $p(d|\mathcal{H})$ serves as normalization constant of the posterior distribution, and is given

Finally, to reduce the Lorentzian contribution to the pre-merger and merger amplitude, we multiply the waveform by a factor $\exp[-i2\pi\Delta t f]$, which will induce a time shift of Δt in the time-domain waveform; Δt is computed as the time interval between the merger and the *first postmerger minimum* described by Eq. (2) in [66].

The frequency-domain gravitational waveform can be written as

$$\tilde{h}(f) = \mathcal{A}(f)e^{i\phi(f)}, \qquad (12)$$

with $\mathcal{A}(f)$ the amplitude and $\phi(f)$ the phase. Therefore, in our model the full waveform is given by:

by

$$p(d|\mathcal{H}) = \int d\vec{\theta}\, p(d|\mathcal{H}, \vec{\theta})p(\vec{\theta}|\mathcal{H}). \qquad (15)$$

Assuming the data d consist of Gaussian noise and a GW signal $h(\vec{\theta})$, the likelihood can be expressed as [75]

$$p(d|\mathcal{H}, \vec{\theta}) \propto exp\left[-\frac{1}{2}\left\langle d - h(\vec{\theta})|d - h(\vec{\theta})\right\rangle\right] \qquad (16)$$

with the noise-weighted inner product defined as

$$\langle a|b \rangle \equiv 4\text{Re} \int_{f_{\text{low}}}^{f_{\text{high}}} \frac{\tilde{a}^*(f)\tilde{b}(f)}{S_n(f)} df, \qquad (17)$$

where $S_n(f)$ is the noise spectral density, $\tilde{a}(f)$ the Fourier transform of $a(t)$, and * denotes the complex conjugate.

To sample the likelihood function, we use the nested sampling [75, 76] package `dynesty` [77, 78], which is included in the `bilby` library [67, 68] .

1. Relative binning

The likelihood evaluations required at each sampling step are very expensive, since, in order to compute the inner product, we need to evaluate the waveform on a

dense and uniform frequency grid. The size of the grid increases both with the duration of the signal and the maximum frequency used in the analysis. In our case, we set $f_{\max} = 4096$ Hz, since the postmerger GW signal is expected to lie within the few kHz regime. Moreover, we study BNS systems, whose low masses imply a long signal duration. Although we set the starting frequency to $f_{\rm low} = 30$ Hz, the typical duration of the signal in band is still roughly 200 s. To overcome the issue of the computational cost of the analysis needed for this work, we employ the technique of relative binning [79, 80], which reduces the number of waveform evaluations from all the points on the grid to a limited number of frequency bins.

The underlying assumption in relative binning is that the set of parameters yielding a non-negligible contribution to the posterior probability produce similar waveforms, such that their ratio varies smoothly in the frequency domain. In each frequency bin $b = [f_{\min}(b), f_{\max}(b)]$, if we choose a reference waveform $h_0(f)$ that describes sufficiently well the data, the ratio with the sampled waveforms can be approximated with a linear interpolation

$$r = \frac{h(f)}{h_0(f)} = r_0(h,b) + r_1(h,b)(f - f_{\rm m}(b)) + \mathcal{O}[(f - f_{\rm m}(b))^2],$$ (18)

with $f_{\rm m}(b)$ the central frequency of the bin b.

This allows to approximate the likelihood inner product as

$$\langle d(f)|h(f)\rangle \approx \sum_b \left(A_0(b) r_0^*(h,b) + A_1(b) r_1^*(h,b) \right),$$ (19)

where the summary data

$$A_0(b) = 4 \sum_{f \in b} \frac{d(f) h_0^*(f)}{S_n(f)/T},$$ (20)

$$A_1(b) = 4 \sum_{f \in b} \frac{d(f) h_0^*(f)}{S_n(f)/T} (f - f_m(b))$$ (21)

are computed on the whole frequency grid, but only for the reference waveform. Also $\langle h(f)|h(f)\rangle$ is calculated with a similar approach. In this method, the evaluation of sampled waveforms is required only to compute the bin coefficients $r_0(h,b)$ and $r_1(h,b)$ in Eq. (18). In this paper, we follow the description and implementation of [79, 81]. To use relative binning with `bilby` inference, we employ the code in [82].

2. Simulations

We test the performance of our model in parameter estimation analysis with simulated signals. We consider three different sources, and analyze them through `bilby` injections, i.e., using our own GW models, and through injecting NR hybrids with the same parameters;

Name	$\mathcal{M}_c$	q	$\tilde{\Lambda}$	Injection
Source1[NR−inj]	1.17524	0.8	604	NR: H_121_151_00155 [87]
Source1[qu−pm]	1.17524	0.8	604	Bilby: quasi-universal
Source1[free−pm]	1.17524	0.8	604	Bilby: free parameters
Source2[NR−inj]	1.08819	1.0	966	NR: H_125_125_0015 [88]
Source2[qu−pm]	1.08819	1.0	966	Bilby: quasi-universal
Source2[free−pm]	1.08819	1.0	966	Bilby: free parameters
Source3[NR−inj]	1.17524	1.0	607	NR: H_135_135_00155 [87]
Source3[qu−pm]	1.17524	1.0	607	Bilby: quasi-universal
Source3[free−pm]	1.17524	1.0	607	Bilby: free parameters

TABLE I. Properties of the sources used for injections. The NR hybrids are taken from the SACRA database [89]. For `bilby` injections, we used our `IMRPhenomD_NRTidalv2_Lorentzian` model, both with quasi-universal relations and with free Lorentzian parameters. In case of injections with the free parameters model, the injected c_0, c_1, c_2 values are obtained from the best fit of the correspondent NR hybrid.

cf. Tab. I. The employed hybrids have a postmerger signal duration of roughly 10 ms.

All simulated signals are injected with zero inclination ι and polarization angle ψ, and with sky location $(\alpha, \delta) = (0.76, -1.23)$. The sky location has been chosen such that none of the employed detector networks is particularly preferred. Depending on the analysis, we performed injections at three different distances: 225 Mpc, 135 Mpc, and 68 Mpc, which, in a network with Advanced LIGO+ and Advanced Virgo+, correspond approximately to a signal-to-noise ratio (SNR) of 30, 50, and 100 respectively. We take priors uniform in $[0.5, 1.0]$ for mass ratio q, and uniform in $[\mathcal{M}_{c,s} - 0.05, \mathcal{M}_{c,s} + 0.05]$ for chirp mass, where $\mathcal{M}_{c,s}$ is the chirp mass of the source, and the prior width is given by the precision on chirp-mass measurements that we anticipate for future detectors. Regarding tidal deformability parameters, we sample over $\tilde{\Lambda}$ and $\Delta\tilde{\Lambda}$, with a prior uniform in $[0, 5000]$ and $[-5000, 5000]$ respectively, where $\Delta\tilde{\Lambda}$ is defined in [90] as

$$\Delta\tilde{\Lambda} = \frac{1}{2}\left[\sqrt{1-4\eta}\left(1 - \frac{13272}{1319}\eta + \frac{8944}{1319}\eta^2\right)(\Lambda_1 + \Lambda_2) \right.$$
$$\left. + \left(1 - \frac{15910}{1319}\eta + \frac{32850}{1319}\eta^2 + \frac{3380}{1319}\eta^3\right)(\Lambda_1 - \Lambda_2)\right],$$ (22)

Luminosity distance priors are uniform in comoving volume, with $D_L \in [1, 450]$Mpc. Although all the sources considered are non-spinning, our baseline model `IMRPhenomD_NRTidalv2` allows for aligned spins; we choose a uniform prior on the spin component aligned with orbital angular momentum $|a_1|, |a_2| \in [0.0, 0.20]$. Finally, when using the postmerger model with free parameters for recovery, we choose uniform priors $c_1 \in$

H: Adv LIGO+ Hanford	V: Adv Virgo+	ET: Einstein Telescope
L: Adv LIGO+ Livingston	K: KAGRA	CE: Cosmic Explorer
I: Adv LIGO+ India	N: NEMO	

2G detectors

3G detectors

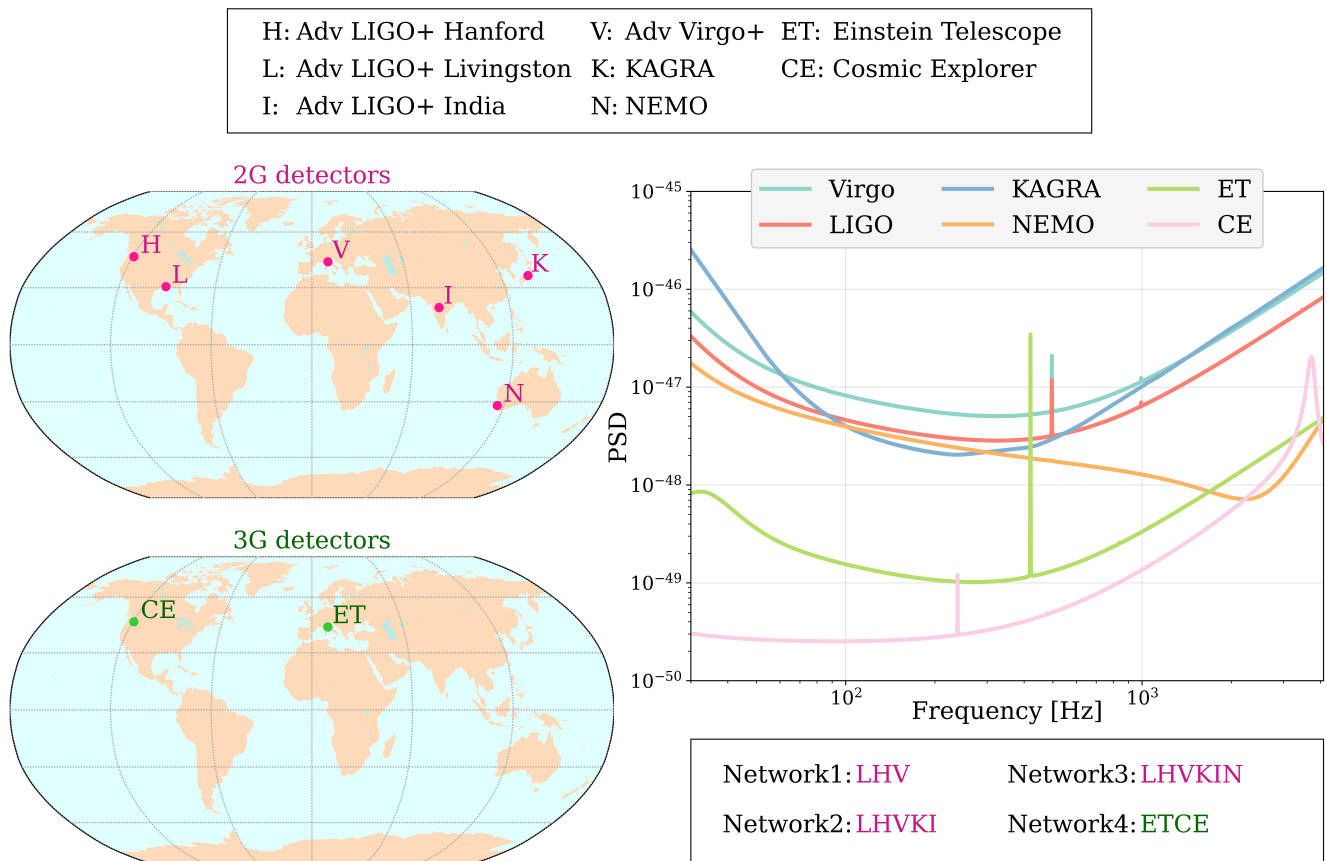| Network1: LHV | Network3: LHVKIN |
| Network2: LHVKI | Network4: ETCE |

FIG. 1. Left: location of the detectors used in this study, top panel for second generation (2G) detectors and bottom panel for third generation (3G) ones. Right: PSDs for the different detectors. The Advanced LIGO+ PSD [83] is used for H, L and I detectors. Since the official sensitivity curve for Advanced Virgo+ is not available yet, we used the same one as for the LIGO detectors, scaled by a factor 4/3 to account for the different arm-length. ET sensitivity is the one referred to as 'ET-D' and given in [84], while CE sensitivity is given in [85]; for KAGRA we use the PSD labeled as 'Combined' in [86].

$[2000, 4096]$ Hz and $c_2 \in [10, 200]$ Hz, while for c_0 we employ a logarithmic uniform prior in $[5 \times 10^{-24}, 1 \times 10^{-22}]$ s^{-1}.

C. Detector Networks

Earth-based GW detectors have the best sensitivity around a few tens to hundreds of Hz, which makes the inspiral and merger signal of coalescing compact objects the perfect candidate for detections. In this work, however, we are interested in the postmerger part of the signal, which is usually weaker and involves higher frequencies. Current detectors are strongly limited at these high frequencies, but the improvements planned for the future detectors' upgrades and the next generation detectors are expected to make postmerger measurements feasible. Therefore, one of the goals of this work is to assess how future detectors can improve the studies we present. We include in our analysis the upgraded versions of existing detectors, Advanced LIGO+, Advanced Virgo+, and KAGRA, as well as new detectors whose construc-

tion has been planned for the next few years, LIGO-India and NEMO, and the next detector generation, Einstein Telescope and Cosmic Explorer. Advanced LIGO+ design [91] will improve the current 4 km arm-length detectors in Hanford (H) and Livingston (L) sites, including a frequency dependent light squeezing and new test masses with improved coating. Advanced Virgo+ (V), similarly, is the planned upgrade for the current Advanced Virgo detector in Cascina [5]. This transition will happen in two separate phases and include upgrades like the introduction of signal recycling and a higher laser power. Advanced LIGO+ and Advanced VIRGO+ are the planned designs for the O5 observing run, which is scheduled to start roughly in 2025, and during which their BNS detection range will reach approximately 330 Mpc and 150-260 Mpc, respectively [92]. KAGRA (K)[93–95] is a 3 km arm-length interferometer built underground in the Kamioka mine in Japan, which already employs innovative technologies like cryogenic mirrors. For O5, its sensitivity at the end of the observing run is predicted to allow a BNS range of at least 130 Mpc [92]. The LIGO network involves a third detector in India (I) [96], which

is currently under construction and is expected to become operative approximately in 2025. Finally, the Neutron Star Extreme Matter Observatory, or NEMO (N), is an Australian proposal for a gravitational-wave detector with 4 km arm-length, specifically designed to have a high sensitivity in the kilohertz band [97]. The possible location of NEMO has not been decided yet, therefore for this work we arbitrary place it at the location shown in Fig. 1. Although not officially approved yet, we include it in our analysis, since its high-frequency sensitivity is particularly interesting for postmerger studies.

3G detectors are expected to increase the sensitivity by a factor between 10 and 30 [92] with respect to current LIGO detectors, but they require the construction of new facilities and are expected to start observing in the mid 2030s. At the moment, the planned 3G detector network includes plans for Cosmic Explorer (CE) in the US and Einstein Telescope (ET) in Europe. CE [24, 25] is planned as an L-shaped interferometer with 40 km arm-length[2]. For the purpose of this paper, we assume it placed at the current Hanford site. ET design [17, 18] includes a so-called 'xylophone' configuration, which guarantees an improved sensitivity at high and low frequencies at the same time [84]. The two candidates for the ET site are Sardinia, in Italy, and Limburg, at the border between the Netherlands, Germany, and Belgium[3]. For this work, we assume ET is placed at the current Virgo site. Although the final design of ET is still under development, here we consider it as a triangular detector, i.e., composed of three V-shaped interferometers with a 60 degree opening angle and 10 km arms.

In this work, we study four different detector networks: HLV, HLVKI, HLVKIN, and ETCE. The detectors' locations and sensitivities are shown in Fig. 1.

III. RESULTS

In the following, we present the results of our simulations, for what concerns both the performance of our model and the improvement we obtain with future detectors. When using the postmerger model with quasi-universal relations, we are mainly interested in studying how well we can recover the tidal deformability parameter $\tilde{\Lambda}$. Since the quasi-universal relations that we derived depend on $\tilde{\Lambda}$, we expect that the postmerger part of the signal, when detected, brings additional information about this parameter. This will likely lead to a narrower posterior with respect to what we can obtain using a model

without postmerger. In the case of the postmerger model with free Lorentzian parameters, we study how well the Lorentzian parameters c_0, c_1, c_2 can be recovered, and especially c_1, since it represents the frequency of the main postmerger emission peak. In the following, we refer to the `IMRPhenomD_NRTidalv2_Lorentzian` postmerger model with quasi-universal relations as QU-PM, to the one with free Lorentzian parameters as FREE-PM, and to the model without postmerger, `IMRPhenomD_NRTidalv2`, as NO-PM.

A. Best-case scenario

We start by testing both versions of our model, FREE-PM and QU-PM, in the best-case scenario, i.e., for `bilby` injections in zero noise, for sources as described in Table I, at a distance of 68 Mpc and with ETCE network. Figure 2 shows the posterior probability density of $\tilde{\Lambda}$ for signals obtained with QU-PM injections, and recovered with both our postmerger models, QU-PM and FREE-PM, and with the model without postmerger NO-PM. As expected, the $\tilde{\Lambda}$ posterior becomes tighter when going from the NO-PM to QU-PM model, with the width of the 90% confidence interval reducing by about 30%, from 23.11 to 15.84 in the case of Source2$_{[qu-pm]}$, and from 15.42 to 11.07 for Source3$_{[qu-pm]}$. In the FREE-PM recovery case, the posteriors becomes wider, with the width of the 90% confidence interval reaching 22.23 and 32.12 for Source2$_{[qu-pm]}$ and Source3$_{[qu-pm]}$ respectively. We also note that when recovering with this model, the median of $\tilde{\Lambda}$ is slightly underestimated with the respect to the injected values. Both these features are predictable due to the higher number of parameters we have to sample over. For Source1$_{[qu-pm]}$, the injected value lies outside the NO-PM $\tilde{\Lambda}$ posterior distribution, but is well recovered with both the QU-PM and FREE-PM models. This is probably due to the fact that injections are performed with a signal with postmerger, and when we recover with a model without the postmerger description, the waveform tries to latch on to the signal after the merger, causing a bias in the parameters estimation.

Figure 3 shows the posteriors for the c_1 Lorentzian parameter in the case of injection and recovery with the FREE-PM model, for the three different sources. The injected values of c_0, c_1, c_2 are the ones that give the best fit on the NR hybrid with the same binary parameters of the source considered. The c_1 parameter, which corresponds to the frequency of the main postmerger emission peak, is well recovered in all cases. Although we are mainly interested in the recovery of c_1, the FREE-PM model provides posteriors also for the c_0 and c_2 parameters, which are related to the maximum amplitude and width of the Lorentzian respectively. Note that the c_0 and c_2 parameters, which are not shown in the figure, are not recovered as well as the c_1 parameter, but they are close to the injected values, as reported in Table II. While our model works for our main purpose of measuring the frequency

---

[2] Recently, also a configuration consisting of a 40 km and an additional 20 km detector has received attention and was considered as the reference concept for the recent Horizon study of [25]. In [98], also a tunable design for the CE detector was proposed, which would enhance sensitivity in the kilohertz band.
[3] In addition, recent interest arose for a third possible site located in the eastern part of Germany.
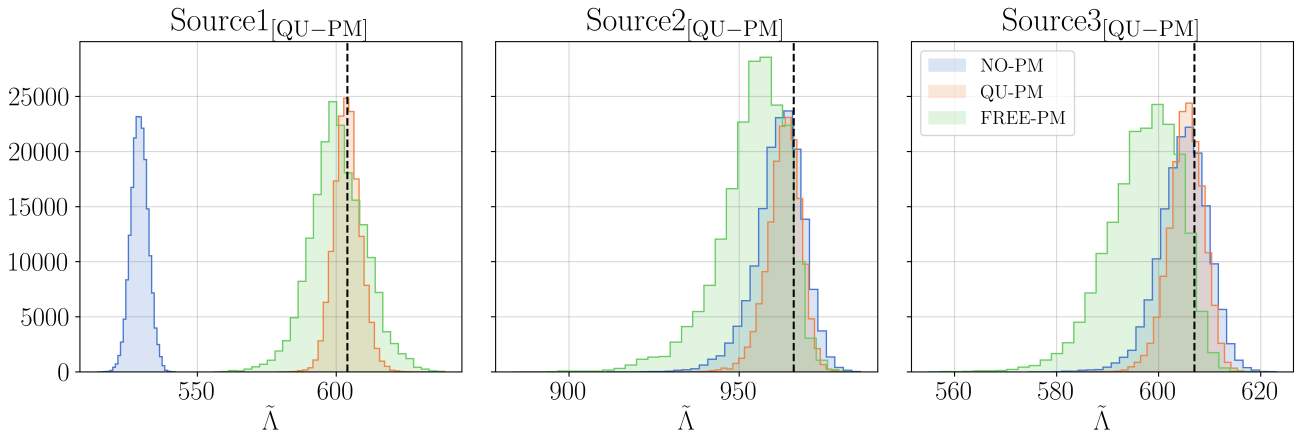
FIG. 2. Posterior probability density for $\tilde{\Lambda}$ in the case of `bilby` injections with the QU-PM model, for sources at 68 Mpc and with the ETCE network, and recovery with the three different models NO-PM, QU-PM and FREE-PM, in blue, orange and green respectively. The black dashed lines correspond to the injected values.
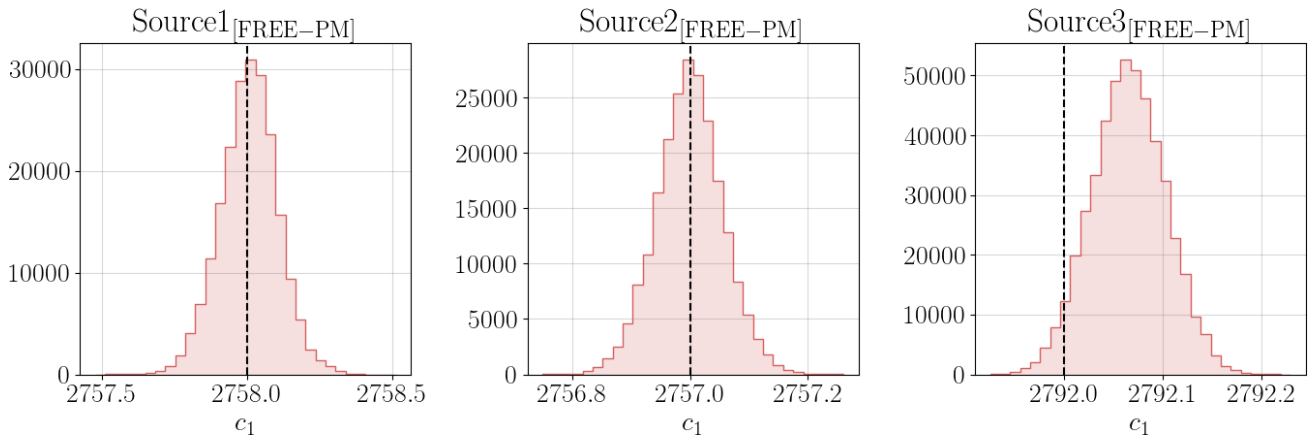

FIG. 3. Posteriors of c_1 parameters for the three different sources, obtained when using the FREE-PM model both for injection and recovery. The black dashed lines show the injected values.

of the dominant postmerger peak, the shifts that we see in the other parameters suggest that we can further improve the FREE-PM model; see e.g. [62, 64] for recent developments including postmerger features beyond the main emission frequency.

B. Detector network performances in zero-noise

We want to investigate how future detector networks will improve our postmerger analysis. For this purpose, we inject signals obtained from the QU-PM model in zero noise, and recover both with the QU-PM and the NO-PM model. We analyze signals injected at three different distances (68 Mpc, 135 Mpc, and 225 Mpc), and we compare results for the four detector networks LHV, LHVKI, LHVKIN, and ETCE (as described in Sec. II C). Due to

	$\log c_0$	$\log c_{0,\text{inj}}$	c_2	$c_{2,\text{inj}}$
Source1$_{[\text{free-pm}]}$	$-51.40^{+0.04}_{-0.03}$	-51.43	$77.0^{+0.18}_{-0.19}$	74.0
Source2$_{[\text{free-pm}]}$	$-51.03^{+0.04}_{-0.03}$	-51.06	$48.0^{+0.1}_{-0.1}$	48.0
Source3$_{[\text{free-pm}]}$	$-50.66^{+0.00003}_{-0.0001}$	-50.70	$39.48^{+0.07}_{-0.06}$	39.0

TABLE II. Median with 5% and 95% quantile values of the posterior probability density for the c_0 and c_2 parameters, together with their injected values, for each of the three sources analyzed, in the case of injection and recovery with the FREE-PM model.

limited computational resources, we look only at two different sources, Source2$_{[\text{qu-pm}]}$ and Source3$_{[\text{qu-pm}]}$.
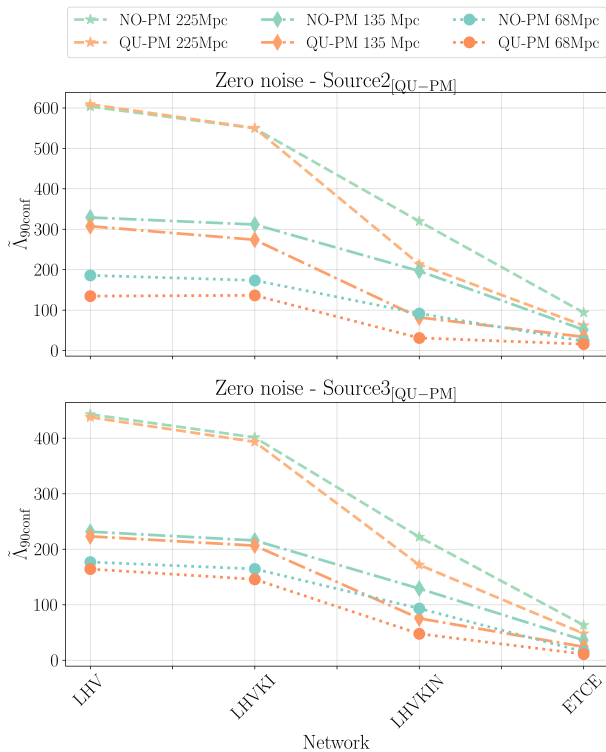Figure 4 shows the uncertainty $\tilde{\Lambda}_{90\text{conf}}$, computed as the

FIG. 4. Width of the 90% confidence interval of $\tilde{\Lambda}$ posterior for Source2$_{[qu-pm]}$ (top panel) and Source3$_{[qu-pm]}$ (bottom panel), as function of the different detector networks. Orange shades represent recovery with the QU-PM model, green shades with the NO-PM one.

width of the 90% confidence interval of the $\tilde{\Lambda}$ posterior probability density, as a function of the detector network employed for the analysis, comparing the different distances and recovery models. As expected, Fig. 4 shows that for all the detector networks considered, and for both models, the width of the 90% confidence interval decreases with decreasing distance. In particular, for an LHV network, we find an improvement of $\sim 50\%$ when going from 225 Mpc to 135 Mpc, and of $\sim 25\%$ (for Source2$_{[qu-pm]}$ even 56%) when going from 135Mpc to 68 Mpc, for both models; for the ETCE network we find an improvement $\sim 45\%$ when going from 225Mpc to 135 Mpc, and $\sim 55\%$ when going from 135 Mpc to 68Mpc. Using the QU-PM model yields to systematically tighter constraints on $\tilde{\Lambda}$, thanks to the additional information arising from the quasi-universal relations that describe the postmerger part of the signal. For both the sources, in the case of injections at 225 Mpc and with the LHV or LHVKI network, we see no significant differences in $\tilde{\Lambda}_{90conf}$ in the case of recovery with the QU-PM or NO-PM model. Considering that such injections generate an SNR $\simeq 30$ in the case of LHV network, this is consistent with the fact that in these situations we do not detect the postmerger signal.

Interestingly, the best improvement when using the QU-PM model comes in the case of LHVKIN network. Going from the LHVKIN to the ETCE network, the constrain on $\tilde{\Lambda}$ improves of about $\sim 70\%$ for both models, while adding NEMO to the LHVKI network leads to an improvement in $\tilde{\Lambda}_{90conf}$ of $\sim 60\%$ for the QU-PM model, against the just $\sim 40\%$ for the NO-PM one. For both sources, we also see that for the LHVKIN network the constraint on $\tilde{\Lambda}$ obtained with the QU-PM model for injections at 135 Mpc is better than the one we retrieve with the NO-PM model for injections at 68 Mpc. 3G detectors are expected to have the best sensitivity over the whole frequency band, and indeed we see that for the ETCE network we get the smallest $\tilde{\Lambda}_{90conf}$ for both models. However, the high sensitivity at lower frequencies allows to obtain a very narrow posterior density distribution for $\tilde{\Lambda}$ from the inspiral part of the signal alone, therefore reducing the impact of the possible information gained from postmerger. In the case of LHVKIN network, instead, the constraint on $\tilde{\Lambda}$ from the inspiral is the one of second-generation detectors, but the high sensitivity of NEMO in the kilohertz band leads to a better detection of the postmerger, and therefore to significantly tighter constraints when using the QU-PM model. If its realization is approved, adding NEMO to the network of second-generation detectors will significantly help the detection of postmerger signals and related studies. We note that for this work we analyze signals with a lower frequency cutoff $f_{low} = 30$ Hz, missing many inspiral cycles; in reality, an additional improvement on $\tilde{\Lambda}$ measurements will be provided by the use of a lower f_{low}.

	Model	$\tilde{\Lambda}_m$ noise$_A$	$\tilde{\Lambda}_m$ noise$_B$	$\tilde{\Lambda}_{inj}$
Source2$_{[qu-pm]}$	QU-PM	$956.68^{+7.08}_{-8.37}$	$959.93^{+6.87}_{-8.71}$	966
	NO-PM	$966.35^{+9.35}_{-11.82}$	$953.10^{+13.11}_{-19.11}$	966
Source3$_{[qu-pm]}$	QU-PM	$608.04^{+11.65}_{-6.27}$	$602.36^{+7.86}_{-12.49}$	607
	NO-PM	$611.76^{+6.68}_{-7.51}$	$604.35^{+6.84}_{-7.70}$	607

TABLE III. Median values with 90% confidence interval for the posterior probability density of $\tilde{\Lambda}$ in case of two different noise realizations, labeled as noise$_A$ and noise$_B$, for injections at 68 Mpc in the ETCE network and for recovery with the two different models QU-PM and NO-PM; the last column reports the injected value of $\tilde{\Lambda}$.

C. Detector Network Performances in non-zero noise

In the previous sections we focused on model and network performances, using injections in zero noise. Now we want to look at the influence of noise on our study. For this reason, we repeat the analysis using Gaussian noise. Due to limited computational resources, we restrict to only two sources, Source2$_{[qu-pm]}$ and Source3$_{[qu-pm]}$, and to one distance, 68 Mpc. We inject signals using the QU-PM model, and recover both with the QU-PM and
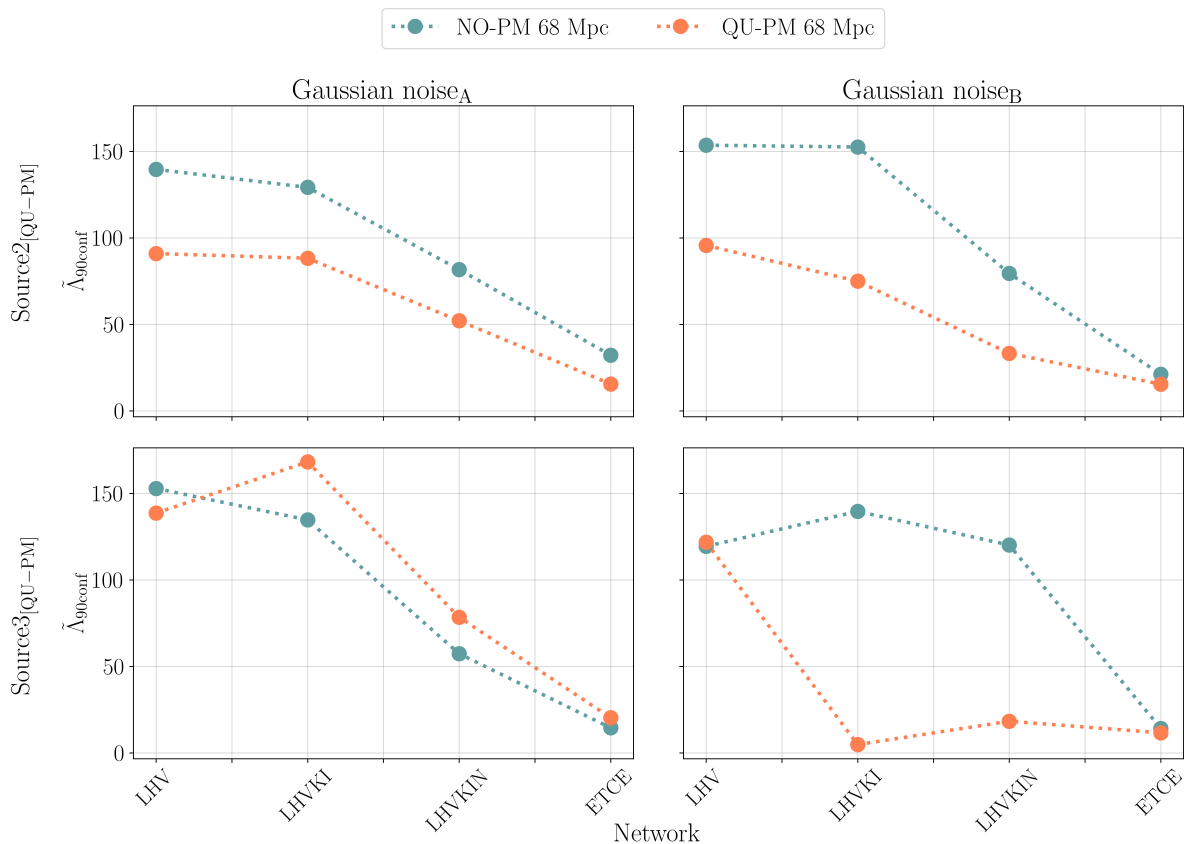
FIG. 5. Width of the 90% confidence interval of $\tilde{\Lambda}$ posterior for Source2$_{[\mathrm{qu-pm}]}$ (top row) and Source3$_{[\mathrm{qu-pm}]}$ (bottom row), as a function of the different detector networks, obtained with two different noise realizations, noise$_\mathrm{A}$ for the left panels, and noise$_\mathrm{B}$ for the right ones.

NO-PM models, comparing results for the different detector networks LHV, LHVKI, LHVKIN, and ETCE. Figure 5 shows $\tilde{\Lambda}_{90\mathrm{conf}}$ for the different detector networks. In order to assess the impact of noise fluctuations, we show results for two different noise realizations, which we call noise$_\mathrm{A}$ and noise$_\mathrm{B}$. Due to the noise impact on the analysis, we do not see the clear trends that we found in the zero noise runs, as described in the previous section Sec. III B. In the case of Source3$_{[\mathrm{qu-pm}]}$ (bottom panels in Fig. 5), with the noise$_\mathrm{A}$ realization the constraints obtained with the QU-PM model are even wider than the ones recovered with the NO-PM model. The most extreme fluctuation is found for Source3$_{[\mathrm{qu-pm}]}$, in the case of LHVKI network and QU-PM model, for which $\tilde{\Lambda}_{90\mathrm{conf}} = 88.26$ in case of noise$_\mathrm{A}$ and $\tilde{\Lambda}_{90\mathrm{conf}} = 4.84$ for noise$_\mathrm{B}$. However, we see that in general $\tilde{\Lambda}_{90\mathrm{conf}}$ decreases with more advanced detectors, with an improvement between 80% and 90% when going from the LHV to the ETCE network. In most cases the QU-PM model allows us to better determine $\tilde{\Lambda}$, although the quantitative improvement strongly depends on the source and especially on the noise realization. Moreover, noise fluctuations impact also the median of the $\tilde{\Lambda}$ posterior probability density, causing different shifts with respect to the injected values (see Table III). Although such shifts appear to be small, they can cause the posterior's median to lie outside the 90% confidence interval, especially in the case of ETCE network, where the $\tilde{\Lambda}_{90\mathrm{conf}}$ is indeed very small.

D. Numerical-relativity injections

Finally, we analyze simulated signals obtained by injecting NR waveforms on top of Gaussian noise. Figure 6 shows the posterior probability density of $\tilde{\Lambda}$, for injections at 68 Mpc in the ETCE network. Although for Source2$_{[\mathrm{NR-inj}]}$ $\tilde{\Lambda}$ is recovered very well, in the other cases we see a shift of the posterior with respect to the injected value of $\tilde{\Lambda}$. For Source1$_{[\mathrm{qu-pm}]}$, the $\tilde{\Lambda}$ injected value lies in the tail of the posteriors recovered with the QU-PM and FREE-PM model, and completely outside the posterior obtained with the NO-PM model; for Source3$_{[\mathrm{qu-pm}]}$, the posteriors recovered with all the models peak at values between 575 and 578, with the injected value $\tilde{\Lambda} = 607$ lying completely outside their distributions. These shifts are due to noise fluctuations, as we showed in Sec. III C, and possible limitations of our waveform models. The case analyzed here, using the ETCE network, generates a signal with a high SNR, and therefore a narrow posterior density for $\tilde{\Lambda}$, with the in-
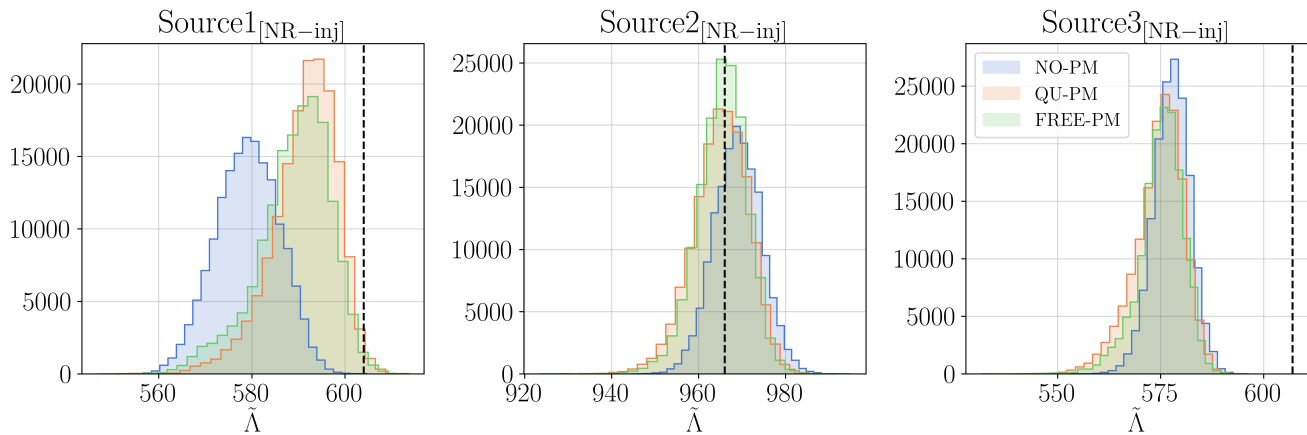
FIG. 6. Posterior probability density for $\tilde{\Lambda}$ as recovered with the different models (NO-PM, QU-PM and FREE-PM) in the case of signals simulated by injecting NR waveforms in Gaussian noise at a distance of 68 Mpc, for the ETCE detector networks. The black dashed lines show the injected values.

jected value resulting outside the 90% confidence interval. Using one of the postmerger models to analyze signals obtained with NR waveforms does not lead to a significant improvement in the $\tilde{\Lambda}$ constraints as the ones shown in Fig. III A. However, for Source1$_{[NR-inj]}$ we see a clear improvement in the recovery of $\tilde{\Lambda}$ with the postmerger model with respect to the one without postmerger, and a modest improvement is also seen for Source2$_{[NR-inj]}$. In Sec. III C, we saw that noise fluctuations alone can impact the performance of our model, but in this case an additional issue is that the NR simulations contain a more complex GW structure in the postmerger, which is not fully recovered with our simple Lorentzian model. For this purpose, both of our QU-PM and FREE-PM models need to be improved towards more structured signals. Moreover, hybridization of NR waveforms starts from the few last cycles of the inspiral, so that also the late-inspiral and merger waveform is based on NR simulations, and thus different from the model we employ. This can lead to biases, affecting the results obtained not only with our FREE-PM or QU-PM models, but also with the model without postmerger.

IV. CONCLUSIONS

We have developed an analytical, frequency-domain model to describe the GW emission during the inspiral, merger, and postmerger phases of a BNS coalescence. For the inspiral and merger, we employed the `IMRPhenomD_NRTidalv2` waveform. We incorporate the postmerger part through modeling the main emission peak with a Lorentzian, whose parameters, in the two versions of our model, are either free or determined by quasi-universal relations. We have shown that both versions work very well in the best-case scenario of high-SNR

and zero noise simulations, leading to better constraints on the $\tilde{\Lambda}$ posteriors and, in the case of the FREE-PM model, to an accurate measurement of the frequency of the main postmerger emission peak. Within our study, we find that noise fluctuations can significantly impact the results. It is important to note that the shifts in $\tilde{\Lambda}$ recovery caused by noise fluctuations, which are evident especially in high-SNR injections, given the narrowing of the posterior, also affect the results obtained with the model without postmerger. Therefore, they must be taken into account in parameter estimation analyses with 3G detectors, even when not related to postmerger studies. In general, including the postmerger during the analysis provides tighter constraints on the $\tilde{\Lambda}$ posterior than the original inspiral-only `IMRPhenomD_NRTidalv2` model. Finally, we used our model to recover signals obtained by injecting NR waveforms. Although we still see improvements in some cases when using the postmerger models, they are not as significant as we found for the simulated signals. This is due to noise effects and the fact that NR waveforms include postmerger signals with a complex structure, which a simple Lorentzian model struggles to recover. Despite the promising results, we conclude that our model, in both its versions, still needs improvements in order to be employed in the analysis of real signals.

Another central point of our study was to assess the performance of different detector networks, and to understand how future detectors will improve the postmerger analysis. In particular, we considered four different networks: (i) Advanced LIGO+ in Hanford and Livingston together with Advanced Virgo+; (ii) the same network as (i) extended by KAGRA and LIGO-India; (iii) the same network as (ii) extended with NEMO; (iv) a network consisting of a 40 km Cosmic Explorer and a 10km, triangular Einstein Telescope. Although 3G detectors, as expected, will give the best constrains on $\tilde{\Lambda}$, we found that NEMO, thanks to its very high sensitivity in the

kiloHertz band, yields the biggest improvement when using the QU-PM model.

Our study showed how, with future detector networks, GW observations from the postmerger phase of a BNS coalescence will allow us to unravel information about the fundamental physics describing supranuclear-dense matter.

Appendix A: Mismatch

The mismatch between two waveforms h_1 and h_2 is defined as

$$MM = 1 - \max_{\phi_c, t_c} \frac{\langle h_1(\phi_c, t_c)|h_2 \rangle}{\sqrt{\langle h_1|h_1 \rangle \langle h_2|h_2 \rangle}}, \qquad \text{(A1)}$$

where t_c and ϕ_c are an arbitrary time and phase shift, and the noise-weighted inner product is as given as in Eq. (17). To validate the IMRPhenomD_NRTidalv2_Lorentzian model, we compute mismatches with the hybrid waveforms in the CoRe [72, 73] and SACRA [89] database. The mismatch is computed with PyCBC [99] functions and zero noise, i.e., with a flat PSD. To get the Lorentzian parameters that better describe each hybrid's postmerger, we optimize the mismatch over c_1, c_2; we do not include the Lorentzian maximum value c_0 in the minimization, because, giving just an amplitude scaling factor, the mismatch is insensitive to it. The initial values for the optimization are found with a least-squares fit on the postmerger part of the hybrid waveform, for
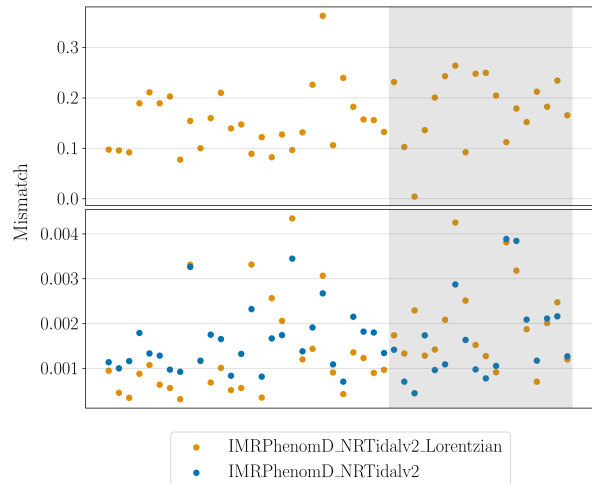

FIG. 7. Mismatches between hybrid waveforms from the CoRe (in the gray-background band) and SACRA database, and our postmerger model IMRPhenomD_NRTidalv2_Lorentzian. The top panel shows mismatches in the postmerger frequency band, i.e., between $[1.1\,f_{\mathrm{merg}}, 4096]$ Hz, the bottom panel for the whole waveform, between $[30, 4096]$ Hz. In the latter case, for comparison we show also mismatches computed between the hybrids and the IMRPhenomD_NRTidalv2 model.

$f \geq 1.3\,f_{\mathrm{merg}}$. Fixing c_1 and c_2 to the optimal values, we then compute the optimal value for c_0 with a least-square fit on the hybrid's postmerger signal. We use the optimal values for the c_i coefficients to generate the IMRPhenomD_NRTidalv2_Lorentzian waveform, for which we compute the mismatch with the hybrid in different frequency ranges. The top panel of Fig. 7 shows the mismatches in the frequency band between $[1.1\,f_{\mathrm{merg}}, 4096]$ Hz: despite our simple model, for almost all hybrids mismatches lie below 0.3. When considering the whole waveform, in the frequency range $[30, 4096]$ Hz, the mismatch is always below 0.005, as shown in the bottom panel of the same figure. For comparison, we show also the mismatches computed in the same frequency range with the IMRPhenomD_NRTidalv2 waveform. The plot does not highlight a systematic improvement in the mismatches when using one of the two models; the difference between the two models' mismatch varies from 0.0019 to 8×10^{-6}, with an average variation of 0.0005. In more than 60% of cases the mismatch is reduced when using the IMRPhenomD_NRTidalv2_Lorentzian model, showing that our postmerger description actually improves the signal characterization.
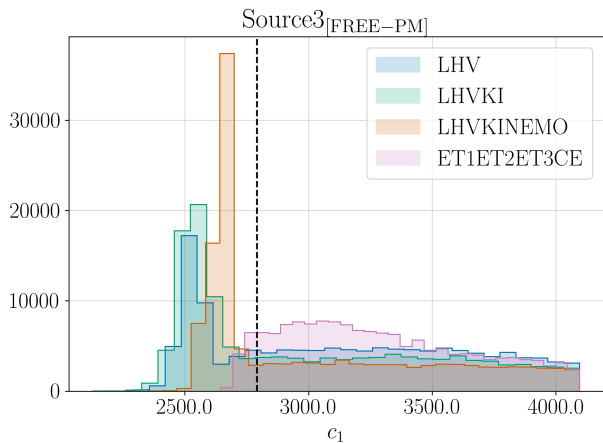
FIG. 8. Posterior probability density for the c_1 Lorentzian parameter for the different detector networks, in the case of Gaussian noise injections at 68 Mpc. The dashed vertical line indicates the injected value.

Appendix B: Results for the free-parameter model

In the following, we show some results obtained with the postmerger model using free Lorentzian parameters. Performing parameter estimation analysis with the FREE-PM waveform requires sampling over three additional parameters, which implies even higher computational costs. For this reason, we could not run the same analyses with the FREE-PM model as we did for the QU-PM one. As shown in Sec. III A, with high-SNR and zero-noise injections, we can recover c_1 accurately. In Fig. 8, we show how different detector networks can recover the c_1 parameter in the case of Gaussian noise injections, for simulated signals corresponding to Source3$_{[free-pm]}$ at 68 Mpc. In the case of second-generation detectors, we see a shift in the peak of the posteriors for the injected value, but we find a clear improvement when adding NEMO. The distribution for the ETCE network is wider but more shifted towards the correct value. We see a plateau in the posterior, extending towards higher frequencies for all the networks. This feature is also present for the ETCE network, for which we recover very precise posteriors in the case of zero noise runs, as shown in Fig. 3. Therefore, we conclude that this is caused by noise fluctuations, which, as reported in Sec. III C, for this source affect quite heavily also the $\tilde{\Lambda}$ measurements. Preliminary studies showed that changing the analysis settings, e.g., fixing c_0 and c_2 to arbitrary values, helps improve the c_1 recovery. Finally, analyses of signals obtained by NR waveforms injections do not recover either of the Lorentzian parameters, because of the complex structure of the postmerger in the NR waveforms, and the noise effects that we see already with simulated signals.

[1] B. P. Abbott et al. (LIGO Scientific, Virgo), Phys. Rev. Lett. **119**, 161101 (2017), 1710.05832.
[2] T. Dietrich, T. Hinderer, and A. Samajdar, Gen. Rel. Grav. **53**, 27 (2021), 2004.02527.
[3] K. Chatziioannou, Gen. Rel. Grav. **52**, 109 (2020), 2006.03168.
[4] J. Aasi et al. (LIGO Scientific), Class. Quant. Grav. **32**, 074001 (2015), 1411.4547.
[5] F. Acernese et al. (VIRGO), Class. Quant. Grav. **32**, 024001 (2015), 1408.3978.
[6] B. P. Abbott et al. (LIGO Scientific, Virgo), Phys. Rev. X **9**, 011001 (2019), 1805.11579.
[7] B. P. Abbott et al. (LIGO Scientific, Virgo), Astrophys. J. Lett. **892**, L3 (2020), 2001.01761.
[8] T. Hinderer, B. D. Lackey, R. N. Lang, and J. S. Read, Phys. Rev. **D81**, 123016 (2010), 0911.3535.
[9] T. Damour, A. Nagar, and L. Villain, Phys. Rev. **D85**, 123007 (2012), 1203.4352.
[10] W. Del Pozzo, T. G. F. Li, M. Agathos, C. Van Den Broeck, and S. Vitale, Phys. Rev. Lett. **111**, 071101 (2013), 1307.8338.
[11] B. D. Lackey and L. Wade, Phys. Rev. **D91**, 043002 (2015), 1410.8866.
[12] M. Agathos, J. Meidam, W. Del Pozzo, T. G. F. Li, M. Tompitak, J. Veitch, S. Vitale, and C. Van Den Broeck, Phys. Rev. **D92**, 023012 (2015), 1503.05405.
[13] T. Dietrich et al., Phys. Rev. **D99**, 024029 (2019), 1804.02235.
[14] K. Kawaguchi, K. Kiuchi, K. Kyutoku, Y. Sekiguchi, M. Shibata, and K. Taniguchi, Phys. Rev. **D97**, 044044 (2018), 1802.06518.
[15] T. Hinderer, Astrophys. J. **677**, 1216 (2008), 0711.2420.
[16] T. Damour and A. Nagar, Phys. Rev. **D81**, 084016 (2010), 0911.5041.
[17] M. Punturo et al., Class. Quant. Grav. **27**, 194002 (2010).
[18] M. Maggiore et al., JCAP **03**, 050 (2020), 1912.02622.
[19] A. Freise, S. Chelkowski, S. Hild, W. Del Pozzo, A. Perreca, and A. Vecchio, Class. Quant. Grav. **26**, 085012 (2009), 0804.1036.
[20] S. Hild, S. Chelkowski, A. Freise, J. Franc, N. Morgado, R. Flaminio, and R. DeSalvo, Class. Quant. Grav. **27**, 015003 (2010), 0906.2655.
[21] B. Sathyaprakash et al., in *46th Rencontres de Moriond on Gravitational Waves and Experimental Gravity* (2011), pp. 127–136, 1108.1423.
[22] C. Pacilio, A. Maselli, M. Fasano, and P. Pani, Phys. Rev. Lett. **128**, 101101 (2022), 2104.10035.
[23] P. K. Gupta, A. Puecher, P. T. H. Pang, J. Janquart, G. Koekoek, and C. Broeck Van Den (2022), 2205.01182.
[24] D. Reitze et al., Bull. Am. Astron. Soc. **51**, 035 (2019), 1907.04833.
[25] M. Evans et al. (2021), 2109.09882.
[26] S. Köppel, L. Bovard, and L. Rezzolla, Astrophys. J. **872**, L16 (2019), 1901.09977.
[27] A. Bauswein, T. W. Baumgarte, and H. T. Janka, Phys. Rev. Lett. **111**, 131101 (2013), 1307.5191.

[28] L. Baiotti, B. Giacomazzo, and L. Rezzolla, Phys. Rev. D **78**, 084033 (2008), 0804.0594.

[29] S. Bernuzzi, Gen. Rel. Grav. **52**, 108 (2020), 2004.06419.

[30] L. Baiotti and L. Rezzolla, Rept. Prog. Phys. **80**, 096901 (2017), 1607.03540.

[31] P. Hammond, I. Hawke, and N. Andersson, Phys. Rev. D **104**, 103006 (2021), 2108.08649.

[32] C. Raithel, V. Paschalidis, and F. Özel, Phys. Rev. D **104**, 063016 (2021), 2104.07226.

[33] E. R. Most, A. Haber, S. P. Harris, Z. Zhang, M. G. Alford, and J. Noronha (2022), 2207.00442.

[34] W. Kastaun and F. Galeazzi, Phys. Rev. D **91**, 064027 (2015), 1411.7975.

[35] A. Bauswein, H. T. Janka, K. Hebeler, and A. Schwenk, Phys. Rev. **D86**, 063001 (2012), 1204.1888.

[36] K. Takami, L. Rezzolla, and L. Baiotti, Phys. Rev. **D91**, 064001 (2015), 1412.3240.

[37] S. Bernuzzi, T. Dietrich, and A. Nagar, Phys. Rev. Lett. **115**, 091101 (2015), 1504.01764.

[38] A. Bauswein and N. Stergioulas, Phys. Rev. **D91**, 124056 (2015), 1502.03176.

[39] B. P. Abbott et al. (LIGO Scientific, Virgo), Astrophys. J. Lett. **851**, L16 (2017), 1710.09320.

[40] B. P. Abbott et al. (LIGO Scientific, Virgo), Astrophys. J. **875**, 160 (2019), 1810.02581.

[41] A. Bauswein, N.-U. F. Bastian, D. B. Blaschke, K. Chatziioannou, J. A. Clark, T. Fischer, and M. Oertel, Phys. Rev. Lett. **122**, 061102 (2019), 1809.01116.

[42] E. R. Most, L. J. Papenfort, V. Dexheimer, M. Hanauske, S. Schramm, H. Stöcker, and L. Rezzolla, Phys. Rev. Lett. **122**, 061101 (2019), 1807.03684.

[43] D. M. Siegel, R. Ciolfi, A. I. Harte, and L. Rezzolla, Phys. Rev. **D87**, 121302 (2013), 1302.4368.

[44] M. G. Alford, L. Bovard, M. Hanauske, L. Rezzolla, and K. Schwenzer, Phys. Rev. Lett. **120**, 041101 (2018), 1707.09475.

[45] D. Radice, Astrophys. J. **838**, L2 (2017), 1703.02046.

[46] M. Shibata and K. Kiuchi, Phys. Rev. **D95**, 123003 (2017), 1705.06142.

[47] R. De Pietri, A. Feo, J. A. Font, F. Löffler, F. Maione, M. Pasquali, and N. Stergioulas, Phys. Rev. Lett. **120**, 221101 (2018), 1802.03288.

[48] A. Bauswein and H. T. Janka, Phys. Rev. Lett. **108**, 011101 (2012), 1106.1616.

[49] S. Bose, K. Chakravarti, L. Rezzolla, B. S. Sathyaprakash, and K. Takami, Phys. Rev. Lett. **120**, 031102 (2018), 1705.10850.

[50] J. Clark, A. Bauswein, L. Cadonati, H. T. Janka, C. Pankow, and N. Stergioulas, Phys. Rev. **D90**, 062004 (2014), 1406.5444.

[51] K. Takami, L. Rezzolla, and L. Baiotti, Phys. Rev. Lett. **113**, 091104 (2014), 1403.5672.

[52] L. Rezzolla and K. Takami, Phys. Rev. **D93**, 124051 (2016), 1604.00246.

[53] K. Hotokezaka, K. Kiuchi, K. Kyutoku, T. Muranushi, Y.-i. Sekiguchi, M. Shibata, and K. Taniguchi, Phys. Rev. **D88**, 044026 (2013), 1307.5888.

[54] A. Bauswein, N. Stergioulas, and H. T. Janka, Phys. Rev. **D90**, 023002 (2014), 1403.5301.

[55] K. Chatziioannou, J. A. Clark, A. Bauswein, M. Millhouse, T. B. Littenberg, and N. Cornish, Phys. Rev. **D96**, 124035 (2017), 1711.00040.

[56] G. Lioutas, A. Bauswein, and N. Stergioulas, Phys. Rev. D **104**, 043011 (2021), 2102.12455.

[57] J. A. Clark, A. Bauswein, N. Stergioulas, and D. Shoemaker, Class. Quant. Grav. **33**, 085003 (2016), 1509.08522.

[58] P. J. Easter, P. D. Lasky, A. R. Casey, L. Rezzolla, and K. Takami (2018), 1811.11183.

[59] M. Breschi, S. Bernuzzi, F. Zappa, M. Agathos, A. Perego, D. Radice, and A. Nagar, Phys. Rev. D **100**, 104029 (2019), 1908.11418.

[60] P. J. Easter, S. Ghonge, P. D. Lasky, A. R. Casey, J. A. Clark, F. H. Vivanco, and K. Chatziioannou, Phys. Rev. D **102**, 043011 (2020), 2006.04396.

[61] T. Soultanis, A. Bauswein, and N. Stergioulas, Phys. Rev. D **105**, 043020 (2022), 2111.08353.

[62] M. Breschi, S. Bernuzzi, K. Chakravarti, A. Camilletti, A. Prakash, and A. Perego (2022), 2205.09112.

[63] M. Breschi, R. Gamba, S. Borhanian, G. Carullo, and S. Bernuzzi (2022), 2205.09979.

[64] M. Wijngaarden, K. Chatziioannou, A. Bauswein, J. A. Clark, and N. J. Cornish, Phys. Rev. D **105**, 104019 (2022), 2202.09382.

[65] T. Dietrich, A. Samajdar, S. Khan, N. K. Johnson-McDaniel, R. Dudi, and W. Tichy (2019), 1905.06011.

[66] K. W. Tsang, T. Dietrich, and C. Van Den Broeck, Phys. Rev. D **100**, 044047 (2019), 1907.02424.

[67] G. Ashton et al., Astrophys. J. Suppl. **241**, 27 (2019), 1811.02042.

[68] I. M. Romero-Shaw et al., Mon. Not. Roy. Astron. Soc. **499**, 3295 (2020), 2006.00714.

[69] N. Stergioulas, A. Bauswein, K. Zagkouris, and H.-T. Janka, Mon. Not. Roy. Astron. Soc. **418**, 427 (2011), 1105.0368.

[70] M. Kölsch, T. Dietrich, M. Ujevic, and B. Bruegmann (2021), 2112.11851.

[71] S. Khan, S. Husa, M. Hannam, F. Ohme, M. Pürrer, X. Jiménez Forteza, and A. Bohé, Phys. Rev. D **93**, 044007 (2016), 1508.07253.

[72] T. Dietrich, D. Radice, S. Bernuzzi, F. Zappa, A. Perego, B. Bruegmann, S. V. Chaurasia, R. Dudi, W. Tichy, and M. Ujevic, Class. Quant. Grav. **35**, 24LT01 (2018), 1806.01625.

[73] http://www.computational-relativity.org/ (2018), CoRe Database webpage.

[74] P. Virtanen, R. Gommers, T. E. Oliphant, M. Haberland, T. Reddy, D. Cournapeau, E. Burovski, P. Peterson, W. Weckesser, J. Bright, et al., Nature Methods **17**, 261 (2020).

[75] J. Veitch and A. Vecchio, Phys. Rev. D **81**, 062003 (2010), 0911.3820.

[76] J. Skilling, Bayesian Analysis **1**, 833 (2006).

[77] J. S. Speagle, Mon. Not. Roy. Astron. Soc. **493**, 3132 (2020), 1904.02180.

[78] S. Koposov, J. Speagle, K. Barbary, G. Ashton, J. Buchner, C. Scheffler, B. Cook, C. Talbot, J. Guillochon, P. Cubillos, et al., *joshspeagle/dynesty: v1.2.2* (2022), URL https://doi.org/10.5281/zenodo.6456387.

[79] B. Zackay, L. Dai, and T. Venumadhav (2018), 1806.08792.

[80] N. Leslie, L. Dai, and G. Pratten, Phys. Rev. D **104**, 123030 (2021), 2109.09872.

[81] L. Dai, T. Venumadhav, and B. Zackay (2018), 1806.08793.

[82] J. Janquart, *RelativeBilbying: a package for relative binning with bilby*, https://github.com/lemnis12/relativebilbying (2022).

[83] L. Barsotti, E. McCuller, M. Evans, and P. Fritschel, *The A+ design curve*, https://dcc.ligo.org/LIGO-T1800042/public (2018).

[84] S. Hild et al., Class. Quant. Grav. **28**, 094013 (2011), 1012.0908.

[85] M. Evans, J. Harms, and S. Vitale, *Exploring the Sensitivity of Next Generation Gravitational Wave Detectors*, https://dcc.ligo.org/LIGO-P1600143/public (2016).

[86] Y. Michimura, K. Komori, Y. Enomoto, K. Nagano, and K. Somiya, *Example sensitivity curves for the KAGRA upgrade* (2020).

[87] K. Kiuchi, K. Kawaguchi, K. Kyutoku, Y. Sekiguchi, M. Shibata, and K. Taniguchi, Phys. Rev. D **96**, 084060 (2017), 1708.08926.

[88] K. Kawaguchi, K. Kiuchi, K. Kyutoku, Y. Sekiguchi, M. Shibata, and K. Taniguchi, Phys. Rev. D **97**, 044044 (2018), 1802.06518.

[89] K. Kiuchi, K. Kawaguchi, K. Kyutoku, Y. Sekiguchi, and M. Shibata, Phys. Rev. D **101**, 084006 (2020), 1907.03790.

[90] L. Wade, J. D. E. Creighton, E. Ochsner, B. D. Lackey, B. F. Farr, T. B. Littenberg, and V. Raymond, Phys. Rev. D **89**, 103012 (2014), 1402.5156.

[91] J. Miller, L. Barsotti, S. Vitale, P. Fritschel, M. Evans, and D. Sigg, Phys. Rev. D **91**, 062005 (2015), URL https://link.aps.org/doi/10.1103/PhysRevD.91.062005.

[92] B. P. Abbott et al. (KAGRA, LIGO Scientific, Virgo, VIRGO), Living Rev. Rel. **21**, 3 (2018), 1304.0670.

[93] T. Akutsu et al. (KAGRA), PTEP **2021**, 05A101 (2021), 2005.05574.

[94] K. Somiya (KAGRA), Class. Quant. Grav. **29**, 124007 (2012), 1111.7185.

[95] Y. Aso, Y. Michimura, K. Somiya, M. Ando, O. Miyakawa, T. Sekiguchi, D. Tatsumi, and H. Yamamoto (KAGRA), Phys. Rev. D **88**, 043007 (2013), 1306.6747.

[96] M. Saleem et al., Class. Quant. Grav. **39**, 025004 (2022), 2105.01716.

[97] K. Ackley et al., Publ. Astron. Soc. Austral. **37**, e047 (2020), 2007.03128.

[98] V. Srivastava, D. Davis, K. Kuns, P. Landry, S. Ballmer, M. Evans, E. D. Hall, J. Read, and B. S. Sathyaprakash, Astrophys. J. **931**, 22 (2022), 2201.10668.

[99] A. Nitz, I. Harry, D. Brown, C. M. Biwer, J. Willis, T. D. Canton, C. Capano, T. Dent, L. Pekowsky, A. R. Williamson, et al., *gwastro/pycbc: Release v2.0.1 of pycbc* (2022), URL https://doi.org/10.5281/zenodo.5825666.